

Geometrical aspects of a hollow-cathode planar magnetron

Zhehui Wang^{a)} and Samuel A. Cohen

Plasma Physics Laboratory, Princeton University, P.O. Box 451, Princeton, New Jersey 08543

(Received 24 September 1998; accepted 16 February 1999)

A hollow-cathode planar magnetron (HCPM), built by surrounding a planar sputtering-magnetron cathode with a hollow-cathode structure (HCS) [Z. Wang and S. A. Cohen, *J. Vac. Sci. Technol. A* **17**, 77 (1999)], is operable at substantially lower pressures than its planar-magnetron counterpart. HCPM operational parameters depend on the inner diameter D and length L of its cylindrical HCS. Only when L is greater than L_0 , a critical length, is the HCPM operable in the new low-pressure regime. The critical length varies with HCS inner diameter D . Explanations of the lower operational pressure regime, critical length, and plasma shape are proposed and compared with a one-dimension diffusion model for energetic electron transport. At pressures above 1 mTorr, Bohm diffusion (temperature \cong primary electron energy), with an ambipolar constraint, can explain the ion–electron pair creation required to sustain the discharge. At the lowest pressure, ~ 0.3 mTorr, collision-limited diffusion creates fewer ion–electron pairs than required for steady state and therefore cannot explain the experimental data. The critical length L_0 is consistent with the magnetization length of the primary electrons. © 1999 American Institute of Physics. [S1070-664X(99)04305-0]

I. INTRODUCTION

A new type of sputtering-magnetron device, called the hollow-cathode planar magnetron (HCPM), has been developed by surrounding a circular planar-sputtering-magnetron (PSM) cathode with a hollow-cathode structure (HCS); see Fig. 1. The HCS is a right cylinder characterized by its length L and inner diameter D . A conventional PSM can be regarded as an extreme of a HCPM, which has $L=0$. HCPMs were found operable at sub-mTorr pressures, depending on the length L . Such low-pressure operation is desirable for certain deposition applications, such as those that require long throw, anisotropic deposition, and low gas incorporation.^{1–4} A larger more uniform plasma volume is generated within the HCPM than in its PSM counterpart. This feature may allow HCPM plasmas to better utilize cathode material.⁵

Details of the experimental apparatus and procedures were described in an earlier paper.⁶ Those experiments employed six different cathode materials, two plasma currents, and HCS of one diameter and three lengths. The experiments described here, in Sec. II, are a more thorough examination of geometry effects over a broader current range for a single target material, copper. In Sec. III we describe the physical processes important to the understanding of the HCPM characteristic, defined as the cathode bias as a function of gas-fill pressure at a constant total cathode current. These characteristics, i.e., voltage ν s. pressure (VP) curves, are the standard by which HCPM performance is evaluated.

Transport in planar magnetrons has attracted much attention.^{7–10} This is the first paper to address electron transport in HCPM. In Secs. III, IV and V, the main processes discussed are the cross-field transport of energetic electrons

created at the cathode by ion and photon impact and the collection efficiency of the cathode for ions formed in the plasma by electron impact ionization.

II. EXPERIMENTAL RESULTS

Both argon and nitrogen plasmas were studied. The HCS in these experiments were made of stainless steel. During PSM operation, the interiors of the HCS are coated by copper, the cathode material. All data taking was performed after the interiors were copper coated. Dimensions of HCS are listed in Table I.

For argon, typical VP characteristics of a HCPM with HCS dimensions $L=10.8$ cm and $D=9.8$ cm are shown in Fig. 2 for fixed total cathode currents $I=20, 50, 100,$ and 300 mA. At pressures between 3 and 30 mTorr, a nearly constant cathode bias of 380 ± 10 V was required to sustain a total cathode current of 300 mA. To maintain the same total cathode current for pressures below 3 mTorr, the cathode bias had to be increased as the pressure was lowered.

VP characteristics for different HCPM dimensions are compared with their PSM counterpart ($L=0$ cm) for an argon plasma with fixed total cathode current $I=300$ mA; see Fig. 3. Three pressure ranges are identified by comparing the PSM VP characteristic with those of the HCPM: high pressure, $p > 13$ mTorr; medium pressure, $1.3 < p < 13$ mTorr; and low pressure, $p < 1.3$ mTorr. The high-pressure range does not show a monotonic relation between V and L . We do not discuss it further in this paper.

In the medium-pressure range, HCPM with greater values of L require less bias voltage than the PSM. As described in more detail in Sec. III, this implies more complete use of the primary electrons' energy, whether directly, through improved electron confinement, or indirectly, through improved ion collection efficiency.

^{a)}Current address: Los Alamos National Laboratory, MS E 526, Los Alamos, New Mexico 87545; electronic mail: zwang@lanl.gov

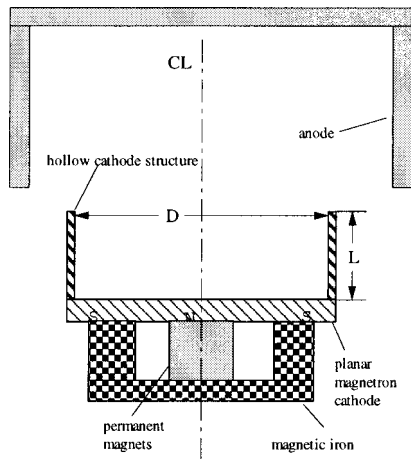


FIG. 1. The schematic of a HCPM configuration. Cathode length L and diameter D are defined.

In the low-pressure range, the conventional ($L=0$) PSM VP characteristic terminates at about 500 V and 1 mTorr, consistent with the results of others.¹¹ HCPM VP characteristics for $L=21.9$, 10.8, and 8.1 cm extend to lower pressure, as low as 0.3 mTorr, and correspondingly higher voltage, about 900 V. For pressures below 1 mTorr and L values of 21.9, 10.8, and 8.1 cm, the HCPM VP curves are within 5% of each other in voltage at the same pressure, with the longer HCS having a slightly lower bias voltage requirement. For $L=5.7$ and 2.5 cm, HCPM VP curves are about the same as the planar magnetron VP curve in terms of the minimum operable pressure.

This set of observations suggests a critical length L_0 , $5.7 \text{ cm} \leq L_0 \leq 8.1 \text{ cm}$, for the fixed HCS diameter $D=9.8 \text{ cm}$. When $L > L_0$, a new and substantially lower-pressure operational regime appears for HCPMs compared with a PSM. The minimum pressures shown in Fig. 3 for different HCS lengths are summarized in Fig. 4. The critical length L_0 is the same for nitrogen discharges, Fig. 4. For a smaller diameter, $D=6.6 \text{ cm}$, the critical length L_0 is also shorter; Fig. 5. In summary, $L_0=6.9 \pm 1.2 \text{ cm}$ for $D=9.8 \text{ cm}$ and $L_0=3.5 \pm 1.0 \text{ cm}$ for $D=6.6 \text{ cm}$.

From these data we calculated the HCS physical aspect ratio, defined as $R_a \equiv L/D$. The critical aspect ratios, when $L=L_0$, are $R_{ac}=0.70 \pm 0.12$ for $D=9.8 \text{ cm}$ and $R_{ac}=0.53 \pm 0.15$ for $D=6.6 \text{ cm}$.

Another result presented previously¹ was the extent of the plasma, determined by the total emissivity (including both gas atom and metal lines) as a function of distance from the cathode surface. In the PSM configuration, the density was highly localized in a typical sputtering magnetron ring within 1 cm of the surface. For the HCPM, the emissivity was radially uniform and extended out to about 10 cm and higher elevations above the cathode.

TABLE I. Dimensions of HCS studied.

L (cm)	21.6	10.8	8.1	5.7	2.5	21.6	10.7	4.5	2.5
D (cm)	9.8	9.8	9.8	9.8	9.8	6.6	6.6	6.6	6.6
$R_a=L/D$	2.2	1.1	0.83	0.58	0.25	3.3	1.6	0.68	0.38

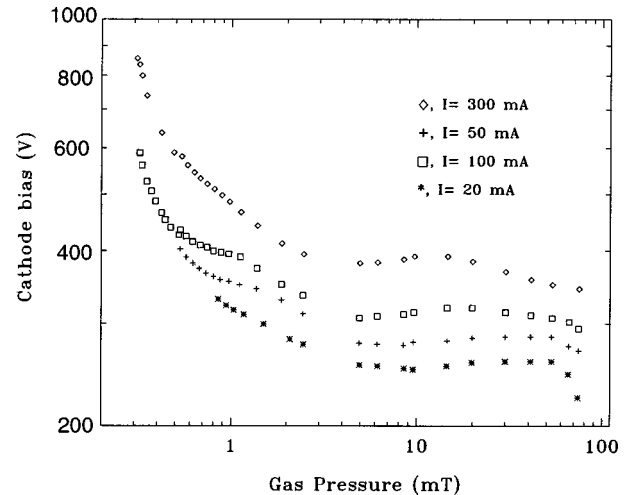


FIG. 2. VP curves for four fixed cathode currents. $L=10.8 \text{ cm}$, $D=9.8 \text{ cm}$, Ar discharge.

III. PARAMETRIC PROPERTIES

Hollow cathode discharges (HCDs) have been studied for a long time.^{12,13} One of the early studies on magnetized hollow cathode discharges was performed by Lidsky *et al.*¹⁴ These employed a uniform magnetic field parallel to the central axis of the hollow cathode tube. The aspect ratio was typically large, $R_a \sim 10$ and the HCS diameter small, $D \sim 1 \text{ cm}$. Furthermore, they operated at elevated temperatures where thermionic emission from the cathode was important. These are quite different from the HCPM parameter range we have studied and are not considered further in this manuscript.

From the HCPM VP characteristics, there are two features that distinguish the HCPM from the PSM: (1) lower operating voltages at medium pressures for the same cathode current; and (2) lower possible operational pressure, though at a higher cathode bias. To understand the causes of these, we examine plasma parameters and phenomena in both the HCPM and the PSM configurations. These are the following:

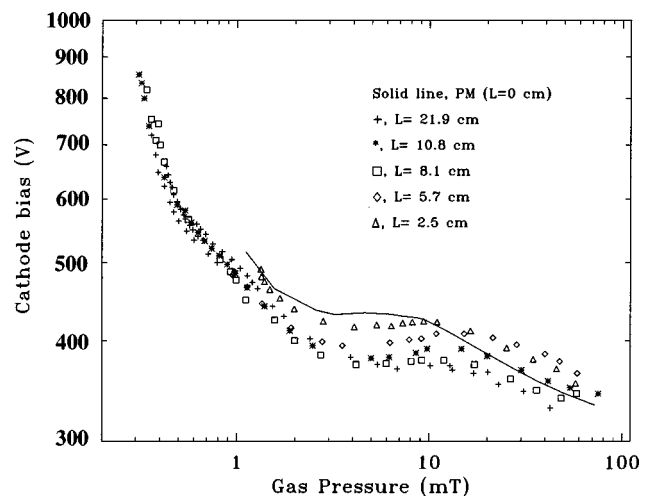


FIG. 3. A comparison of VP curves for $D=9.8 \text{ cm}$ and five different values of L . The Ar discharge, $I=300 \text{ mA}$.

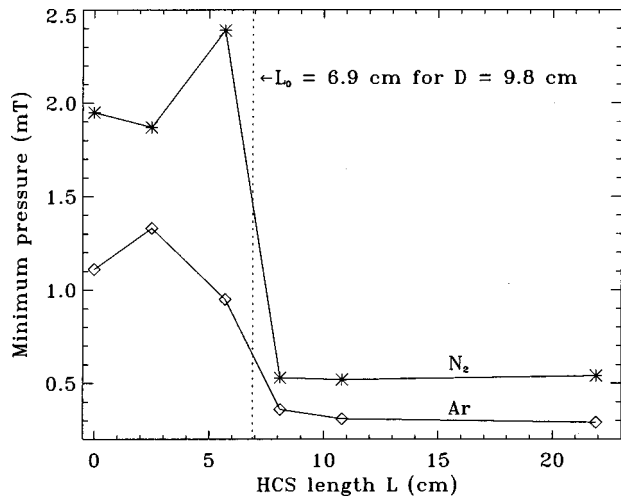


FIG. 4. A HCS critical length $L_0=6.9\pm 1.2$ cm was found for both Ar and N_2 discharges when $D=9.8$ cm. Cathode current $I=300$ mA.

charged-particle motions, charged-particle-wall interactions, and charged-particle collisions with neutral gas particles.

A. Charged-particle motion

In this section, we estimate the effects of the static magnetic and electric fields on the motion of the electrons and ions. The maximum vacuum magnetic field was measured to be 170 ± 10 G at the surface of the cathode and about 60 G 1 cm above that point. The detailed magnetic field distribution was calculated using the ANSYS code,¹⁵ Fig. 6 and Fig. 7, and confirmed by Hall probe measurements.

HCPM plasmas, similar to PSM ones, are sustained by primary electrons that originate from ion- and photon-induced secondary electron emission by the cathode. The secondary electrons are emitted with initial energy of about 5 eV. When secondary electrons move across the cathode sheath, they become energetic primary electrons within the plasma. Their large energy, typically 400–900 eV in these HCPM experiments, came from the cathode bias. By ionization of the working gas, these primary electrons create so-

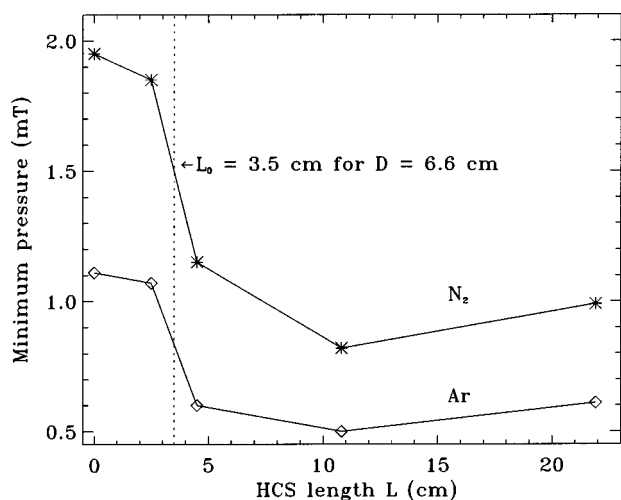


FIG. 5. A HCS critical length $L_0=3.5\pm 1.0$ cm was found for both Ar and N_2 discharges when $D=6.6$ cm. Cathode current $I=300$ mA.

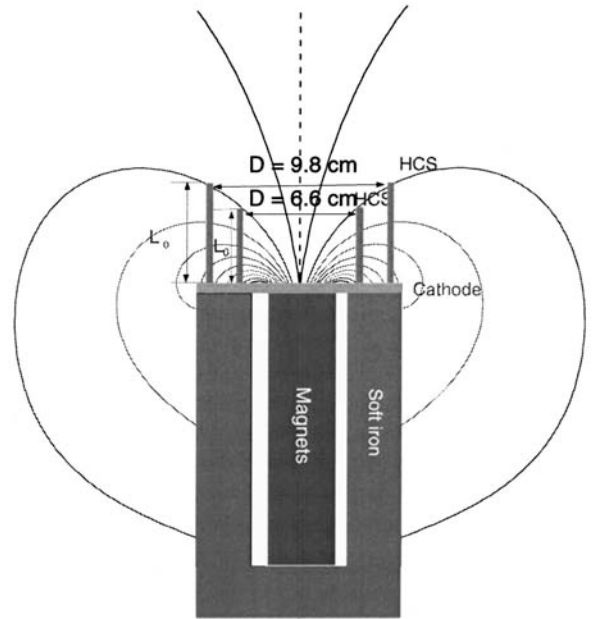


FIG. 6. An extended magnetic field configuration of the HCPM.

called *ultimate* electrons. The ultimate electrons have a quasi-thermal distribution with a temperature near 3 eV.¹¹

At the maximum field, a room-temperature Ar^+ ion has a gyroradius of 0.6 cm. Ion heating due to collisions with electrons can be neglected due to the mass difference. Ions can be heated to higher temperatures primarily through charge exchange with the neutral gas heated by sputtered neutrals and backscattered/neutralized working gas. These indirect processes generally are more important than direct collisions with the sputtered neutral atoms, which usually have energies of a few eV.¹⁶ Higher ion energies means a larger *Larmor* radius than 0.6 cm. Because of this large value of the Ar^+ gyroradius, within the plasma ions may move toward or away from the cathode surface, little affected by the magnetic field. Within the plasma, the static electric field, E , should be less than the background *ultimate* electron temperature divided by the local scale length. The potential difference in an ion-ion-collision mean-free path is very small, hence E should also not affect ion motion. At the plasma

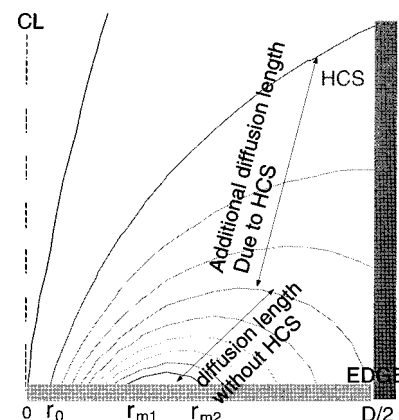


FIG. 7. A detailed HCPM magnetic field configuration, showing the definitions of different regions on the cathode surface.

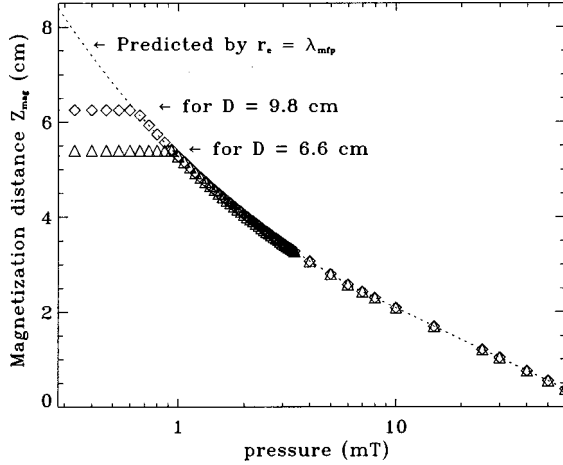


FIG. 8. The magnetization distance of energetic electrons. Regions below the curves are where the primary electrons are magnetized.

boundaries, both near and away from material surfaces, ions will be accelerated to the ion acoustic speed, set by the energy of the escaping electrons. This constraint has a profound effect on the plasma transport, as discussed in Sec. IV.

The relatively cool ultimate electrons have gyroradii less than 1 mm, and hence are fully magnetized, even where the magnetic field falls to 10 G. They are constrained to closely follow the magnetic field lines on helical orbits. They are reflected by the cathode sheath electric field when they approach the cathode surface. A first-order correction to their motion is drift across the magnetic field by $\mathbf{E} \times \mathbf{B}$ and B gradient and curvature.¹⁷

The primary electrons, with energies of 400 eV or more, initially have gyroradii up to 0.5 cm depending on the relative orientation of the motion to the magnetic field. Because of their high energy, their zeroth-order motion includes the drifts across B caused by $\mathbf{E} \times \mathbf{B}$ and B gradient and curvature. These electrons also oscillate back and forth along B between the sheaths. In the absence of collisions, drift motion would form a closed loop around the magnetron axis.¹⁷ However, due to collisions and field fluctuations, these primary electrons may diffuse across magnetic field lines away from the cathode surface toward the edge of the cathode and toward the anode. This diffusive transport motion is second order near the cathode surface but becomes first order a few cm above the surface.

Because the magnetic field is nonuniform and decreases with the elevation Z above the cathode, we can introduce a criterion for the magnetization of electrons as

$$r_e < L \equiv \text{Min}(\lambda_{\text{mfp}}, D/2). \quad (1)$$

Here r_e is the electron Larmor radius. λ_{mfp} is the mean-free path of the electron-neutral collisions. Here D is the diameter of the HCS. For electrons to be magnetized, their Larmor radii r_e should be smaller than these dimensions. We are particularly interested in primary electrons with energy on the order of several hundred eV. At such high energy, the dependence of the collision rate on energy can be neglected, $\langle \sigma_i \nu \rangle = 4.0 \times 10^{-7} \text{ cm}^3/\text{s}$ for Ar gas. The solutions for Eq. (1) are illustrated in Fig. 8, based on magnetic field calculated

with the ANSYS code. The dashed line curve corresponds to $r_e = \lambda_{\text{mfp}}$. The region below the curve is where electrons are considered magnetized. At low pressures, the HCS radius sets the distance beyond which the electrons are not magnetized. For $D = 9.8 \text{ cm}$, the magnetization length for electrons $Z_{\text{mag}} = 6.25 \text{ cm}$, while for $D = 6.6 \text{ cm}$, $Z_{\text{mag}} = 5.40 \text{ cm}$. The relation of the magnetization length to the critical length of the HCPM L_0 is discussed in Sec. V.

B. Energy balance and particle transport

The power supplied to the magnetron is

$$P_{\text{PS}} = I_T V_c, \quad (2)$$

where V_c is the cathode bias voltage. Here $I_T = I_+ (1 + \gamma + \langle \gamma_p \rangle)$ is the total current, I_+ is the ion current to the cathode, γ is the secondary electron emission coefficient due to ion bombardment, $\langle \gamma_p \rangle \equiv \sum \gamma_v G_v N_v / G N_i$ represents the averaged secondary electron emission due to UV photons. The summation is over different wavelengths. A detailed discussion of collection efficiency coefficients G and G_v , particle numbers N and N_v will be given in Sec. V A. (The anode is assumed to be at ground potential.) As in a dc glow discharge, most of the energy input into the magnetron is quickly converted to heating the cathode by ion bombardment,

$$P_c = I_+ V_c, \quad (3)$$

where we have ignored the extremely small cathode cooling by secondary electron evaporation and assumed that the potential drop in the plasma is zero. The difference between Eqs. (2) and (3) is the power input into the plasma available to cause ionization, creating ultimate electrons,

$$P_e = P_{\text{PS}} - P_c = I_+ V_c (\gamma + \langle \gamma_p \rangle) = I_+ V_c \gamma_{\text{eff}} \sim 0.3 I_+ V_c, \quad (4)$$

where $\gamma_{\text{eff}} \equiv \gamma + \langle \gamma_p \rangle \sim 0.3$, as described in Sec. V A. We have assumed $G_v / G \sim 1$. Not all this power will be consumed by ionization and excitation events. Some power may be deposited on the anode by electron impact, if the mean ionization and excitation times are longer than the primary-electron confinement time. In Sec. IV we evaluate this condition quantitatively.

For argon, creation of an ultimate electron consumes about 40 eV of a primary-electron's energy. About 16 eV is for the actual ionization process and 24 eV for excitation processes prior to ionization.¹⁸ (For these energetic primary electrons, very little energy is lost via bremsstrahlung, elastic collisions with neutrals, or Coulomb scattering on the ultimate electrons or the ions.) Thus, if a 400 eV primary electron deposited most its energy in the plasma prior to impacting the anode, it would create about ten electron-ion pairs. For ion impacts on the cathode to be solely responsible for sustaining the discharge, $\gamma = 0.1$ is required. As will be discussed in Sec. V A, below 500 eV, γ is smaller than this by about a factor of 2, supporting the interpretation that photon impacts are important for generating about half the primary electrons.

For the largest value of γ_{eff} , approximately 0.3, primary electrons would have to deposit about 120 eV in the plasma to sustain a steady state.

Examination of Figs. 2 and 3 show that low-pressure operation requires higher cathode bias voltage. Higher cathode voltages cause higher ion impact energies and higher γ values (to 0.1 at 1 keV). A comparison of energy-dependent excitation and ionization rates shows a constant fraction of electron energy being used for excitation versus ionization at higher electron energies. We conclude that, for low-pressure HCPM operation, the energetic electrons are lost prior to their using all their energy creating ultimate electrons.

We next examine the combined effects of electron energy loss and transport, comparing Bohm-like transport with neutral- and Coulomb-collision transport, all limited by the ambipolar constraint. These three mechanisms can cause plasma transport across the magnetic field, away from the cathode surface. If transport is rapid enough, the fast electrons can be lost to the anode prior to using their full energy for ionization and excitation.

An electron's confinement on a flux surface can be disrupted by collisions with neutral particles, charged particles, and oscillatory electric and magnetic fields within the plasma. These three mechanisms result in collisional, classical (Coulomb collisions), and Bohm transport across the magnetic field. The relative importance of collisional to classical transport is measured by R_{ne} , the ratio of Coulomb collision frequency to the electron-neutral collision frequency:

$$R_{ne} = \frac{\nu_{ei}}{\nu_{en}}, \quad (5)$$

where $\nu_{en} = n_0 \sigma_i \sqrt{T_e/m_e}$, n_0 is the neutral density, and σ_i is the average electron-neutral total collision cross section at electron temperature T_e . Inserting the expression for $\nu_{ei} \equiv 3.9 \times 10^{-6} n_i Z^2 \ln \Lambda T_e^{-3/2} = 3.9 \times 10^{-6} n_e \ln \Lambda T_e^{-3/2} \text{ s}^{-1}$, where the quasineutrality assumption $Zn_i = n_e$ and the single-ionization assumption $Z=1$ are used, R_{ne} is found to be

$$R_{ne} = 9.3 \times 10^{-14} \frac{n_e \ln \Lambda}{n_0 \sigma_i T_e^2}. \quad (6)$$

For most of laboratory plasmas and glow discharges¹⁹ $\ln \Lambda = 12$; then

$$R_{ne} = 1.1 \times 10^{-12} \frac{n_e}{n_0 \sigma_i T_e^2}. \quad (7)$$

Typical magnetron discharges are partially ionized, i.e., $n_e/n_0 = 10^{-2} - 10^{-3}$ (ionization fraction). For the ultimate electrons, $T_e = 3 \text{ eV}$ and $\sigma_i = 10^{-16} \text{ cm}^2$, giving $R_{ne} = 1$ to 10, which means both electron-electron collisions and electron-neutral collisions are important for electrons with thermal energy T_e . In contrast, primary electrons, with their higher energy, have a thousand-fold weaker Coulomb scattering and a five-times larger σ_i . Hence, for them, Coulomb collisions with the background plasma are unimportant relative to collisions with neutrals.

We now compare the collisional diffusion coefficient, D_C , to the Bohm diffusion coefficient, D_B , defining the ratio $R_{CB} \equiv D_B/D_C$,

$$D_C = \rho_e^2 \nu_{en}, \quad (8)$$

$$D_B = 6 \times 10^6 T(\text{eV})/B(\text{G}), \quad (9)$$

$$R_{CB} = 5 \times 10^{13} B/n_0 / \sqrt{T_e}, \quad (10)$$

where we have used $5 \times 10^{-16} \text{ cm}^2$ as the cross section for scattering of 400 eV electrons by neutral argon. At $p = 10 \text{ mTorr}$, $B = 100 \text{ G}$, and $T_e = 400 \text{ eV}$, $R_{CB} = 1$; at 1 mTorr and the same B and T_e , $R_{CB} = 10$. Hence Bohm diffusion, if operative, would dominate the fast electron losses as well as the cooler electrons losses at low pressures.

C. Minimum operation pressure of a HCPM

Here we present a heuristic picture of the physics that sets the minimum pressure. In Sec. IV we examine results from a one-dimensional (1-D) numerical model showing a comparison between the predicted minimum pressure for the three transport mechanisms just discussed.

In the model, electrons are launched with a fixed energy from the cathode. They eventually are lost to the anode wall. In between the cathode and the anode, electrons undergo diffusive motion. The boundary conditions of this diffusive motion at the cathode is of the reflecting type, while that at the anode is of the absorbing type. In other words, the primary electron density gradient is zero at the cathode and maximum at the anode.²⁰ The whole diffusion region is of length L_0 , the same as the HCS length. If we assume the diffusion coefficient D to be constant in space, then the solution to the steady-state diffusion equation, which gives the electron density distribution n_e as a function of the elevation z above the cathode surface, is

$$n_e = n_0 \left(1 - \frac{z}{L_0} \right), \quad (11)$$

where n_0 is the plasma density on the cathode surface. The average time for an electron to diffuse to $z=L_0$ is $\tau = L_0^2/2D$. The minimum operating pressure, or corresponding neutral density n_0 , can be estimated from the time it takes a energetic primary electron to diffuse a distance $z=L_0$ out of the HCPM system. The pressure can only be so low that when an primary electron diffuses out of the HCPM, the average diffusion time, equal to $L_0^2/2D$, should be greater than $(\gamma_{\text{eff}})^{-1}$ times the ionization time $(\nu_i)^{-1}$,

$$\tau = \frac{L_0^2}{2D} > 1/(\gamma_{\text{eff}} \nu_i) \sim 3/\nu_i, \quad (12)$$

where we have assumed $(\gamma_{\text{eff}})^{-1} = 3$. This allows sufficient numbers of electron-ion pairs to be formed to sustain the discharge in steady state, as discussed in Sec. V.

Using $\langle \sigma_i \nu \rangle = 2 \times 10^{-7} \text{ cm}^3/\text{s}$ as the ionization rate coefficient for 40–400 eV electrons, we find the ionization frequency $\nu_i (\text{s}^{-1}) = 2 \times 10^{-7} n_0 (\text{cm}^{-3})$ and obtain

$$n_0 > D/(3 \times 10^{-8} L_0^2). \quad (13)$$

For a Bohm diffusion coefficient appropriate to the parameters of the primary electrons in the HCPM, $T_e \geq 300$ eV, $B \leq 100$ G, and $L_0 = 6.9$ cm, this yields a minimum density,

$$n_0 \geq 1 \times 10^{13} \text{ cm}^{-3}, \quad (14)$$

comparable to the observed value. And as readily inferred from the values of R_{CB} and R_{ne} , in no region of density will Coulomb collisions predict the proper n_0 , while a diffusion coefficient appropriate to neutral collisions can fit, based on this heuristic picture.

These estimations are based on an overly simplified model and conservative values for all the parameters involved. A detailed calculation will be presented in Sec. IV.

D. Cathode erosion profile and plasma shape

It is observed in PSMs that cathode erosion is most rapid and the plasma density and emissivity greatest where the local magnetic field is nearly parallel to the cathode surface. Hence, there the ions and photons responsible for secondary emission are most plentiful; secondary electrons are emitted primarily from there. At that position, the sheath electric field is nearly perpendicular to the magnetic field. This region lies between $r_{m1} \leq r \leq r_{m2}$, shown in Fig. 7.

The width and location of this region were studied by Wendt and Lieberman²¹ for PSMs. For HCPM operation at pressures greater than 10 mTorr, an electron born where B is parallel to the surface accelerates away from the cathode a distance equal to the gyroradius, $r_e \propto V_{\text{sheath}}^{1/2}/B$, approximately 0.5 cm for a bias of about 500 V. These electrons may move along B and are reflected deep in the cathode sheaths that have thickness $\sim \lambda_D (V/T_e)^{3/4} \sim 0.1$ cm.¹⁸ The motion along B sets the sputter trench width \bar{w} . It is determined geometrically by the electron gyroradius n_e and the radius of the curvature of the magnetic field line that is tangential to the cathode, a . Wendt and Lieberman found

$$\bar{w} = 2\sqrt{2ar_e}, \quad (15)$$

when the sheath thickness is small compared with the electron gyroradius, equivalent to a plasma dielectric constant.

From the discussion in Sec. III C, at pressures greater than 10 mTorr, $R_{CB} \leq 1$, hence primary electron transport is dominated by collisions and it is appropriate to use D_C , Eq. (8), as the vertical transport coefficient. As an order-of-magnitude estimation, it was found that the vertical diffusion length Z is determined by $Z = r_e \sqrt{E/U_0}$ for a primary electron to loss all of its energy. For $E = 500$ eV, $U_0 = 40$ eV, Z is about 1.8 cm. From the ANSYS code calculation of the magnetic field distribution, it is seen that the B -field line there starts and ends at the main cathode surface, not the HCS. Therefore all the primary electrons starting where B is tangential to the cathode lose their energy without reaching the HCS. Ionization mainly takes places in the small volume at where B is parallel and close to the cathode. The cathode erosion profile, as we observed experimentally at pressures above 10 mTorr, can be explained by the PSM model, as developed by Wendt and Lieberman.

In the sub-mTorr pressure range accessible only to the HCPM, the primary electrons have a much longer mean-free

path and a higher energy from the higher cathode bias (about 1 kV). The higher energy causes the primaries to reach more distant field lines and to retain their energy longer. For Bohm as well as collisional diffusion, the lower B at these higher elevations and higher energy further promote more rapid diffusion away from the cathode. Electrons moving along more distant magnetic field lines are confined electrostatically, by reflection from HCS. Ionization takes place in a larger volume than that at high pressures. Ion bombardment occurs over a larger cathode surface area. \bar{w} , as observed experimentally, is much larger than estimated using the PSM model.

IV. ONE-DIMENSION DIFFUSION MODEL

In this section, we present a one-dimension (1D) diffusion model for primary electron energy deposition in an Ar HCPM discharge. The dimension of interest here is the elevation above the cathode surface: z . At the cathode surface, $z = 0$.

The diffusion equation for steady state is

$$\frac{d}{dz} \left(D \frac{dn}{dz} \right) = \frac{I_e}{e} \delta(z), \quad (16)$$

where e is the elementary charge. I_e , the cathode electron emission current, is related to the total cathode current, as discussed in Sec. III.

The average primary electron energy as a function of elevation is derived as the following: Energy loss is assumed to be by ionization and excitation alone with a rate given by

$$dE/dt = -n_0 \langle \sigma_i v_e \rangle U_0, \quad (17)$$

where E is in eV and U_0 is the energy loss for the creation of each ion–electron pair; we assume it to be 40 eV for simplicity. The ionization cross section data for Ar was taken from McDaniel.²² Using the drift speed of the particle,

$$v_d = \frac{dz}{dt}, \quad (18)$$

Eq. (17) becomes

$$\frac{dE}{dz} = -\frac{1}{v_d} n_0 \langle \sigma_i v_e \rangle U_0. \quad (19)$$

The drift speed is also given by

$$v_d = -D \frac{1}{n} \frac{dn}{dz}. \quad (20)$$

We are interested in the solution of the above diffusion equation from $z = 0$ to L . As discussed in Sec. III A, L corresponds to the magnetization distance, beyond which the magnetic field has no effect on electron motion. We can pose two kinds of boundary conditions at $z = L$ to the above diffusion equation. (1) an unrestricted-flow boundary condition; the drift velocity is equivalent to electron kinetic energy at $z = L$; and (2) an ambipolar-limited boundary condition, where the maximum electron drift speed is the ion-acoustic velocity, C_s .

Case 1 corresponds to

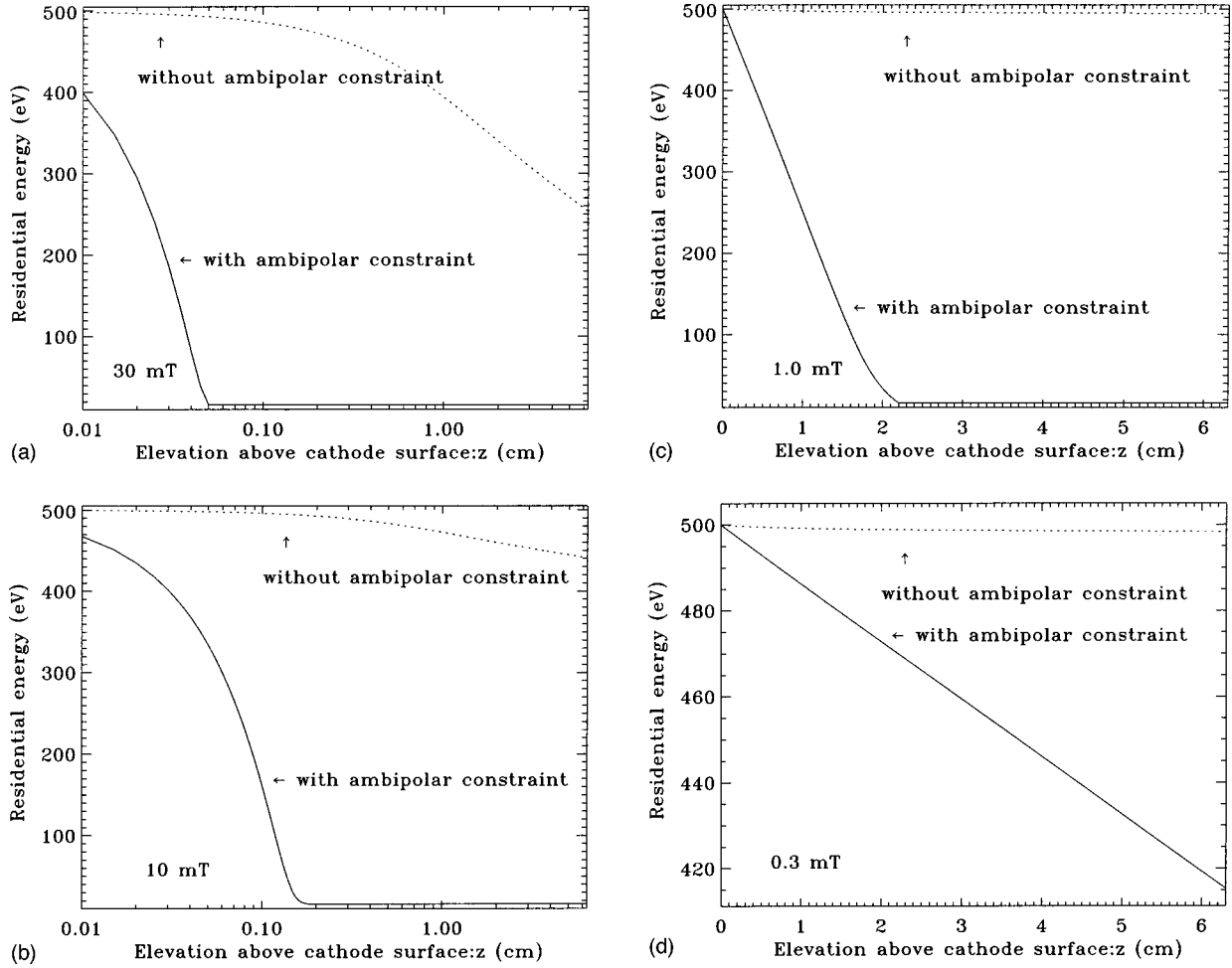


FIG. 9. A calculation of the residual energy of electrons as a function of the elevation above the cathode. Bohm and ambipolar-limited Bohm transport were modeled for electrons with an initial energy of 500 eV. Energy loss is by ionization and excitation. Four different pressures were modeled. (a) 30 mTorr, (b) 10 mTorr, (c) 1 mTorr, (d) 0.3 mTorr. Gyroradius effects are not included.

$$v_d = v_L \equiv \sqrt{\frac{2E(z=L)}{m_e}}, \quad \text{at } z=L. \quad (21)$$

A solution of the diffusion equation gives

$$n(Z) = \frac{I_e}{e} \frac{1}{v_L} + \frac{I_e}{e} \int_z^L \frac{dz}{D},$$

$$\frac{1}{v_d} = \frac{1}{v_L} + \int_z^L \frac{dz}{D}, \quad (22)$$

for $0 \leq z \leq L$.

Case (2) corresponds to

$$v_d = C_s \equiv 9.79 \times 10^5 \sqrt{\frac{\gamma E(z=L)}{\mu}}, \quad \text{at } z=L. \quad (23)$$

in cm/s. For our case, $\gamma=3$ and $\mu=40$ for Ar. The solution is identical to Eq. (22), with v_L replaced by C_s .

Because the magnetic field and primary electron energy vary with position, the diffusion coefficient $D=D(z)$ is position dependent. We numerically solve the diffusion equation with either boundary condition. The numerical model includes the magnetic field as a function of elevation above the cathode surface from the ANSYS code. Due to the 2-D

nature of the magnetic field, the field strength used in our calculation is approximated to be $B(z) = B(z, (rm_1 + rm_2)/2)$, values over the sputter trench.

The data shown are for an $L=6.9$ cm HCS, which corresponds to HCS $D=9.8$ cm. Similar calculations were performed for $D=6.6$ cm. The calculated residual energies for 500 eV primary electrons are shown in Figs. 9(a)–9(d) as a function of elevation above the cathode for the Bohm transport assumption, with and without the ambipolar constraint and with the temperature set to one-half the primary electron energy. The choice of the starting energy for primary electrons at 500 eV is based on our experimental observation that for most of the pressure ranges above 1 mTorr, VP curves are nearly independent of voltage at about 500 eV.

Each figure is for a different neutral density: 1.1×10^{13} , 3.6×10^{13} , 3.6×10^{14} , and $10.8 \times 10^{15} \text{ cm}^{-3}$, corresponding to gas pressures of 0.3, 1, 10, and 30 mTorr. For all pressures, ‘‘pure’’ Bohm diffusion without an ambipolar constraint at the boundary is too rapid to explain the electron energy loss rate that is required to sustain the discharge. For a gas pressure of 30 mTorr, 10 mTorr, ambipolar-limited Bohm transport results in energy lost within ~ 0.1 cm of the cathode, a distance on the order of the plasma sheath. This

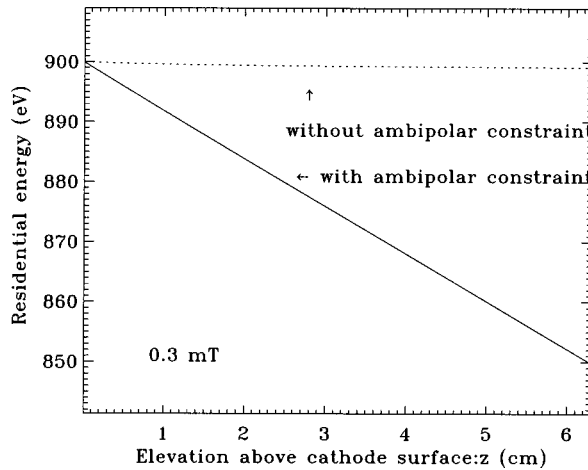


FIG. 10. A calculation of the residual energy of electrons as a function of elevation using Bohm and ambipolar-limited Bohm transport for electrons with an initial energy of 900 eV at 0.3 mTorr.

distance is physically unreasonable, since it is shorter than ρ_e . For cases where transport is slow, ionization will occur at $\pm \rho_e$.

At 1.0 mTorr, the distance for electrons that lose their energy is substantially larger, about 2 cm. However, at an experimental value of minimum operating pressure of 0.3 mTorr, the primary electrons lose only ~ 85 eV if the ambipolar-limited Bohm transport is operable, not enough to sustain the discharge. Therefore ambipolar-limited Bohm transport simulation can explain the energy loss to pressure as low as 1 mTorr reasonably well, however, it cannot explain experimental data at sub-mTorr.

Low-pressure simulations were performed for higher-energy primary electrons. Figure 10 shows the results for 900 eV primaries at 0.3 mTorr. At the critical length, $L = 6.3$ cm. Primaries can lose only about 50 eV for the Bohm type of diffusion with the ambipolar constraint.

A similar set of runs was made for collisional transport; see Fig. 11. At a gas pressure of 0.3 mTorr, the result is similar to the Bohm type. Because the collisional-limited dif-

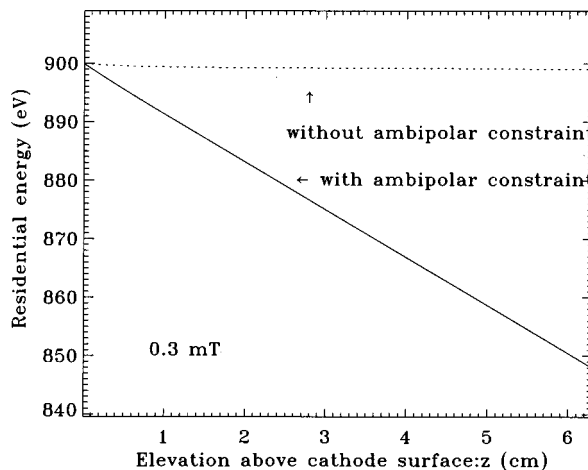


FIG. 11. A calculation of the residual energy of electrons as a function of elevation using collisional diffusion for electrons with an initial energy of about 900 eV at 0.3 mTorr.

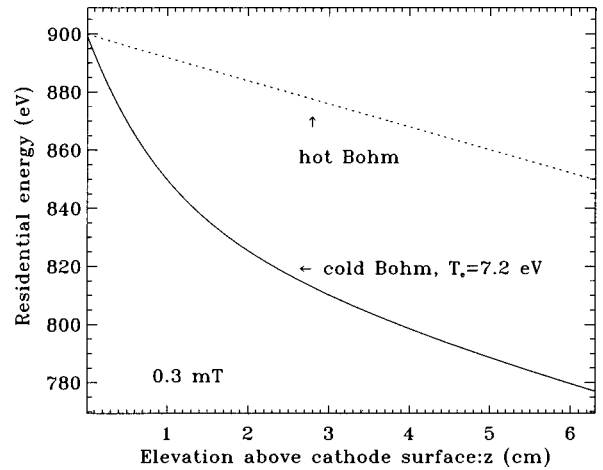


FIG. 12. A calculation of the residual energy of electrons as a function of elevation using a Bohm diffusion coefficient with fixed $T_e = 3$ eV, for primary electrons with an initial energy of about 900 eV at 0.3 mTorr.

fusion gives the lower limit in transport speed for any transport process, this result gives us a dilemma to be resolved, either by a more realistic model (higher dimension), or there are some interesting physics to be explored.

One attempt, which cannot be justified by sound physical reasons, was through using Bohm diffusion coefficients with a bulk electron temperature of up to about 7.2 eV, so-called "cold" Bohm diffusion. The energy loss of the primaries can be about 120 eV at the critical length; Fig. 12.

A summary comparing these results with the experiment is in Table II. "Yes" means that adequate energy loss within the observed distance is predicted by the code to match the experiments.

V. HOLLOW-CATHODE EFFECTS

Built upon the results of the diffusion model, we start this with a statement of the sufficient condition to sustain a discharge, i.e., the generation of sufficient secondary electrons at the cathode to replenish those lost by transport. Hollow-cathode effects, such as improvements upon ion-collection efficiency, are estimated. An explanation for the critical length, which is related to lower operation pressure for a HCPM is obtained.

A. A sufficient condition

A steady-state HCPM discharge replenishes energetic primary electrons lost by transport to the anode and by en-

TABLE II. A comparison of results using different diffusion models with experimental data.

	500 eV 1, 10, 30 mTorr	900 eV 0.3 mTorr
Pure "Bohm"	No	No
Bohm+ambipolar	Yes	No
Collisional	No	No
Collisional+ambipolar	Yes	No
'Cold Bohm'+ambipolar	Yes	Yes

ergy loss (*via* ionization, excitation, elastic scattering, or particle–wave interactions) into the distribution of ultimate electrons.

For each primary electron lost, the number of ion–electron pairs created, N_i , is described by

$$N_i = \int_0^x n_0 \sigma_i dy, \quad (24)$$

where n_0 is the neutral gas density and σ_i is the (energy-dependent) cross section for ionization. The integration is along the trajectory of the electron. Here x is called the pathlength of the primary electron, which is the length of the actual electron trajectory, not the guiding center, which starts from where the electron is born (cathode) to where the electron disappears (such as the anode).

Similarly, the number of energetic (UV) photons created N_ν at frequency ν is

$$N_\nu = \int_0^x n_0 \sigma_\nu dy, \quad (25)$$

where σ_ν is the excitation cross section.

A sufficient condition for steady state in a HCPM plasma is the replenishment of primary electrons described by

$$\gamma N_i G + \sum_\nu \gamma_\nu N_\nu G_\nu = 1, \quad (26)$$

where the summation is over the different frequencies of the energetic photons emitted. Here G is the ion-collection efficiency of the cathode and G_ν is the photon-collection efficiency of the cathode for photon frequency ν . In addition, γ is the secondary emission coefficient for an ion striking the cathode, and γ_ν is the secondary emission coefficient for a photon striking the cathode. The left-hand side of Eq. (26) stands for effects that can, on average, replace the loss of a primary electron. The first term on the left-hand side (lhs) is the amount of secondary electrons generated due to ion bombardment. The second term on the lhs is the amount of secondary electrons generated due to UV photons of all wavelengths. For steady state, the lhs=rhs (right-hand side).

For Ar^+ striking Cu, the value of γ is ~ 0.05 from 0 to 500 V and then rises linearly to 0.1 at 1 keV.²³ For the Ar resonance lines (916.7 and 1085.7 Å), the value of γ_ν is nearly constant at 0.1; for the 1199 Å resonance line, γ_ν drops to 0.04.²⁴ From these, we estimate the ratio $R_{iv} \equiv N_i/N_\nu \sim 0.5$, i.e., about twice as many UV photons are created as ion–electron pairs due to the ratio of ionization to excitation cross sections. Here G and G_ν are positive quantities that are equal to or less than 1. Increases of G and G_ν are readily expected due to the change in HCS geometry, discussed in Sec. VB.

Inserting Eqs. (24) and (25) for N_i and N_ν yields the condition sufficient for steady state:

$$n_0 \left(\gamma G \int_0^x \sigma_i dy + \sum_\nu \gamma_\nu G_\nu \int_0^x \sigma_\nu dy \right) = 1. \quad (27)$$

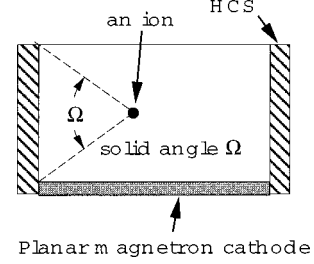


FIG. 13. The increasing utilization of ions in a HCPM, due to an increase in the solid angle of Ω , which is determined by the position where the ion is born, and the area of the HCS.

B. Collection efficiencies

The HCS increases the ion and photon collection efficiencies, G and G_ν . An ion or photon born within the plasma may move in any direction, depending upon its arbitrary initial velocity vector. Without a HCS many ions and photons do not reach the planar magnetron cathode and are lost without the creation of secondary electrons. For an ion (or photon) born at a position $(r_0, 0, Z_0)$ in cylindrical coordinates from the cathode, the probability of its reaching the cathode, or the cathode collection efficiency is determined by a solid angle of the cathode subtended from that position:

$$G = \frac{1}{4\pi} \int_0^{2\pi} d\theta \int_0^{R_0} \frac{Z_0 r dr}{(Z_0^2 + r_0^2 + r^2 - 2rr_0 \cos \theta)^{3/2}}. \quad (28)$$

Here $R_0 = D/2$ is the inner radius of the HCS. For $r_0 = 0$, the integration can be worked out analytically as

$$G = \frac{1}{2} \left(1 - \frac{Z_0}{(Z_0^2 + R_0^2)^{1/2}} \right). \quad (29)$$

For $Z_0 \ll R_0 = 4.9$ cm, $G = 50\%$. For $Z_0 = 1.5$ cm, $G = 35\%$. For r_0 other than zero, the integration can be calculated numerically. For example, $R_0 = 4.9$ cm, $r_0 = 2.0$ cm and $Z_0 = 1.5$ cm, $G = 33\%$.

In a HCPM, those ions (and photons) that reach the HCS will produce additional secondary electrons. The increase in G (or G_ν) is determined by the solid angle of the HCS subtended at where the ion (photon) is born, as illustrated in Fig. 13. The total solid angle determined by areas of the HCS and the cathode with respect to the position of the ion \tilde{G} is

$$\tilde{G} = 1 - \frac{1}{4\pi} \int_0^{2\pi} d\theta \int_0^{R_0} \frac{(L - Z_0) r dr}{[(L - Z_0)^2 + r_0^2 + r^2 - 2rr_0 \cos \theta]^{3/2}}, \quad (30)$$

where L is the HCS length. Again, for $r_0 = 0$, the integration can be solved analytically as

$$\tilde{G} = \frac{1}{2} \left(1 + \frac{L - Z_0}{[(L - Z_0)^2 + R_0^2]^{1/2}} \right). \quad (31)$$

When $Z_0 \ll R_0 = 4.9$, $L = 6.9$ cm, $\tilde{G} = 91\%$. The net increase in collection efficiency due to HCS is $\Delta G = \tilde{G} - G = 91\% - 50\% = 41\%$. For $Z_0 = 1.5$ cm, $\Delta G = 52\%$. For r_0 other than zero, the integration can be calculated numerically. For example, $r_0 = 2.0$ cm and $Z_0 = 1.5$ cm, $\Delta G = 51\%$.

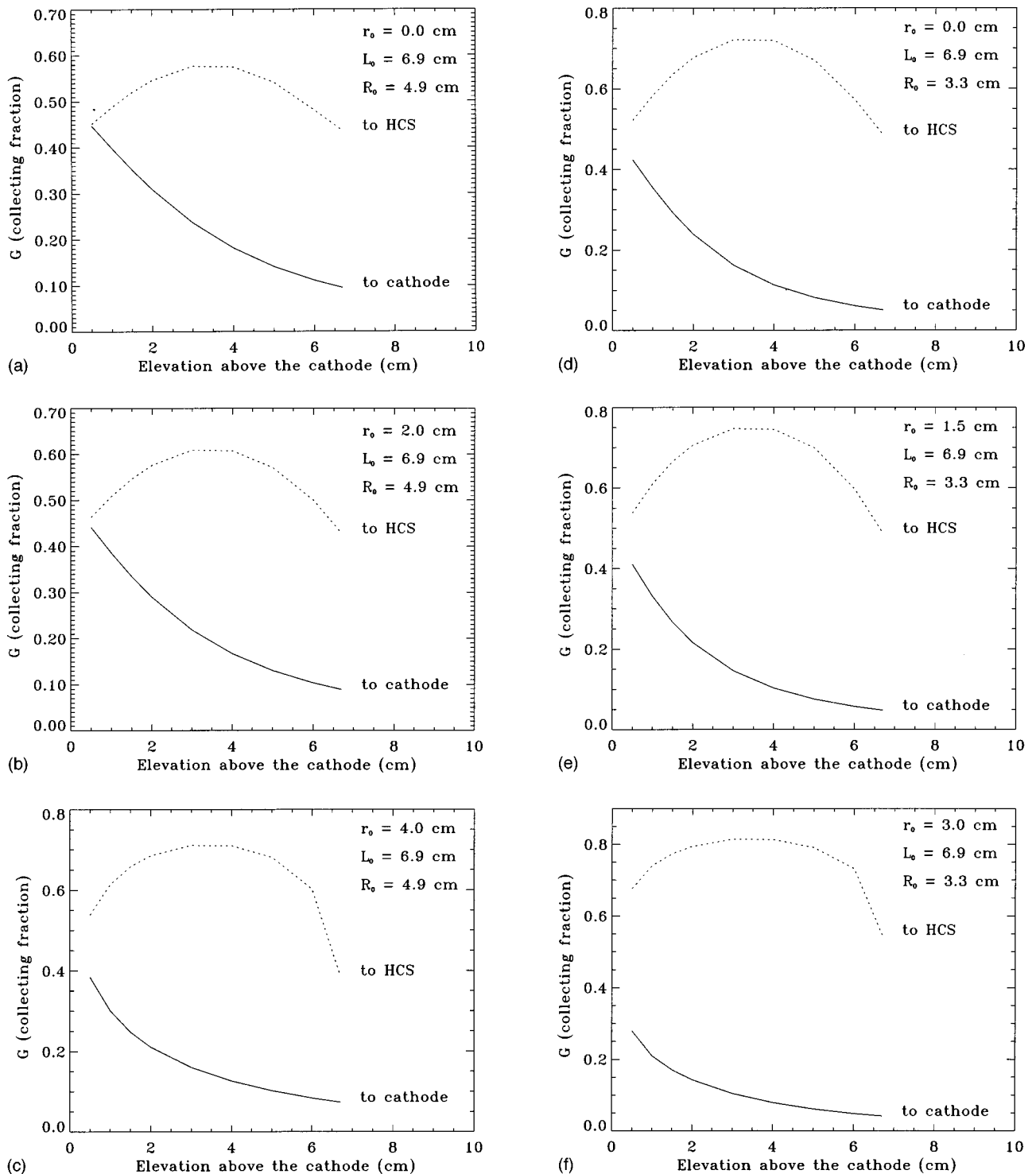


FIG. 14. The calculation of ion and photon collection efficiency by the HCS and cathode, respectively, assuming solid angle effects only. Electric field effects are not included.

Numerical calculations of G and ΔG dependence upon the ion elevation above the cathode are shown in Figs. 14(a)–14(f). In the calculations, $L=L_0=6.9$ cm are used. Figures 14(a)–14(c) are for $R_0=4.9$ cm and ion radius $r_0=0.00, 2.0,$ and 4.0 cm, while Figs. 14(d)–14(f) are for $R_0=3.3$ cm and ion radius $r_0=0.0, 1.5,$ and 3.0 cm. Figures 14(a)–14(c) are for $R_0=4.9$ cm and on radius $r_0=0.0, 2.0,$ and 4.0

cm. These values of $L, R_0, r_0,$ and Z_0 are typical for our HCS configuration.

From the numerical result, we see that HCS has a collection efficiency ranging from 40%–80%, while the cathode has one ranging from 10%–50%. From our earlier measurements¹ of current distribution between the cathode and HCS, for pressures greater than 10 mTorr, the total cur-

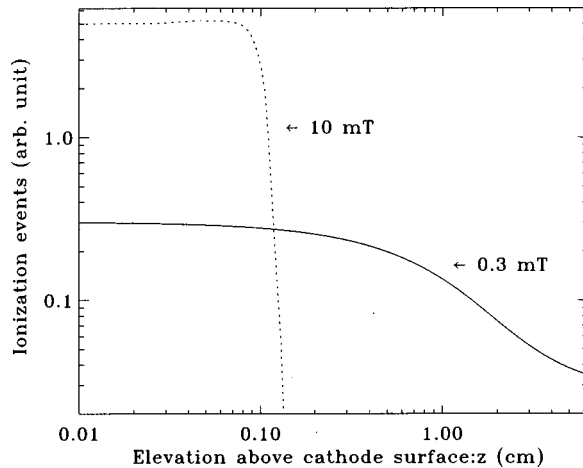


FIG. 15. Ionization events as a function of elevation for low and high pressures.

rent from HCS accounts for only about 15% of the total cathode current, or the ratio of the HCS current to that of the cathode is 20%. To explain the experimental data, knowledge of the number of ionizations as a function of position is needed, in addition to the collection efficiency. Figure 15 shows the distributions of ionization events from the 1-D diffusion model for two pressures, 10 and 0.3 mTorr. At a pressure of 10 mTorr, ions are mostly created within a distance of 0.1 cm, the same order of magnitude as the cathode sheath. Because such an ionization region is close to the cathode, the sheath electric field is probably important to modify the ions from a simple isotropic distribution once they are created. They will preferentially go to the cathode, explaining why the sidewall current is only about 20% of the cathode current. In the lower-pressure case, 0.3 mTorr, the ionization events occur at higher elevations. Accordingly, the HCS will collect more cathode current than at higher pressures, as observed experimentally.

C. Critical length L_0

The previous sections showed that the addition of HCS to a PSM (1) provides an electrostatic barrier for primary electrons following magnetic field lines that intersect with HCS; (2) provides primary electrons an additional drift length to slow down and deposit their energies through collisions with neutrals; and (3) improves the collection efficiency of the ions and UV photons. All these effects may contribute to setting the value of L_0 .

Consider the magnetic field distribution first. In a HCPM there is an area surrounding the cathode center, $0 \leq r \leq r_0$, Fig. 7, where the magnetic field is perpendicular to the cathode surface and whose field lines do not intercept the HCS. There, $\mathbf{E} \parallel \mathbf{B}$ and primary electrons are lost in their first transit (10^{-7} s) to the vacuum chamber wall. All other field lines intersect the HCS or cathode. Primary electrons originating from $r > r_0$ are electrostatically confined by the HCS. To obtain a value of r_0 , we choose a length for each HCS diameter, and then follow a field line from the remote edge of the HCS to the cathode; see Fig. 6. In this way, we see how

r_0 varies with L and D . This, however, does not give insight to what relates r_0 to L_0 .

In Sec. III A, we discussed how the electron magnetization length depends on the discharge pressure. At lower pressures, electrons are magnetized farther away from the cathode surface compared with that at higher pressures because of less collisions with neutrals. Primary electrons are magnetized up to $Z_{\text{mag}} = 6.25$ cm for $D = 9.8$ cm and $Z_{\text{mag}} = 5.40$ cm for $D = 6.6$ cm. These numbers give a clear physical link to the experimental critical length data. An extension of the HCS to a length longer than Z_{mag} essentially operates the discharge far away from the cathode in a low-aspect-ratio unmagnetized hollow-cathode discharge mode.

In Sec. IV, we have modeled the primary electron diffusion out of the discharge system. The model shows that at pressures of more than 1 mTorr, ambipolar-limited diffusion processes can slow down primary electron diffusion, promoting rapid energy loss from their initial ~ 500 eV value to bulk electron energy of a few eV within a distance of 1 cm or less. The HCS does not play a significant role for this high-pressure case. However, for sub-mTorr pressures, additional drift length due to the HCS is needed to create sufficient ionization events to sustain the discharge. The critical length is set by the diffusive loss rate. The diffusive loss rate depends on the magnetic field. Among the various diffusion mechanisms discussed, ambipolar-limited Bohm diffusion with a rate determined by the bulk electron temperature up to 7.2 eV can explain the critical length, as observed experimentally.

VI. SUMMARY AND CONCLUSION

Through measurements of HCPM VP characteristics as functions of HCS dimensions, we have identified a critical length L_0 for fixed HCS inner diameter D beyond which hollow-cathode effects are most strong and substantially lower-pressure operation is possible.

The pattern of cathode erosion due to ion bombardment can be explained by the PSM model for HCPM pressure greater than 10 mTorr. However, at low pressures accessible only to HCPMs, a larger cathode erosion area, as observed experimentally, is expected.

Hollow cathode effects on the ion and UV collection efficiency are estimated from the solid angle calculations. A 40%–80% collection efficiency increase due to HCS is expected, depending on the ion birth position. It is necessary to have better knowledge of the electric field distribution in a HCPM to explain the current distribution between the HCS and the cathode. Because the electric field affects the primary electron drift motion, it also modifies the motion of ions.

The minimum operating pressure is related to the primary electron energy deposition in the plasma. The energy deposition is set by the electron transport. Our model makes similar assumption about energetic electron collisions, as in previous works.^{7–10} Our emphasis is on electron transport mechanisms in the nonuniform HCPM magnetic field. A baseline diffusion transport speed determined by collisions does not give sufficient ion–electron pair creation, as

observed experimentally. In contrast, Bohm diffusion, with a coefficient set by the bulk electron temperature, can adequately describe the data in all pressure ranges.

The existence of a critical length L_0 for sub-mTorr operation is discussed based on primary electron motion in the magnetic field configuration. Collisions with neutrals, and therefore gas pressure, are important to affect the value of L_0 . Here L_0 is consistent with the magnetization length of the electron.

ACKNOWLEDGMENTS

We thank Dr. Zhihong Lin and Dr. D. P. Stotler for useful discussions.

This work is supported by U.S. Department of Energy Contract No. DE-AC02-76-CHO-3073

- ¹S. M. Rossnagel, D. Mikalsen, H. Kinoshita, and J. J. Cuomo, *J. Vac. Sci. Technol. A* **9**, 261 (1990).
- ²P. F. Cheng, S. M. Rossnagel, and D. N. Ruzic, *J. Vac. Sci. Technol. B* **13**, 203 (1995).
- ³Z. J. Radzinski, W. M. Posadowski, S. M. Rossnagel, and S. Shingubara, *J. Vac. Sci. Technol. B* **16**, 1102 (1998).
- ⁴J. Musil, A. Rajskey, A. J. Bell, J. Matous, M. Cepera, and J. Zeman, *J. Vac. Sci. Technol. A* **14**, 2187 (1996).
- ⁵Y. Ohtsu, Y. Tsurume, and H. Fujita, *Rev. Sci. Instrum.* **69**, 1833 (1998).
- ⁶Z. Wang and S. A. Cohen, *J. Vac. Sci. Technol. A* **17**, 77 (1999).
- ⁷T. E. Sheridan, M. J. Goeckner, and J. Goree, *J. Vac. Sci. Technol. A* **8**, 30 (1990).
- ⁸M. J. Goeckner, J. A. Goree, and T. E. Sheridan, *IEEE Trans. Plasma Sci.* **19**, 301 (1991).
- ⁹A. E. Wendt, M. A. Lieberman, and H. Meuth, *J. Vac. Sci. Technol. A* **6**, 1827 (1988).
- ¹⁰T. E. Sheridan, M. J. Goeckner, and J. Goree, *J. Vac. Sci. Technol. A* **16**, 2173 (1998).
- ¹¹J. L. Vossen and W. Kern, in *Thin Film Processes* (Academic, New York 1978), p. 96.
- ¹²F. Paschen, *Ann. Phys. (Leipzig)* **4**, 901 (1916).
- ¹³J.-L. Delcroix and A. R. Trindade, *Adv. Electron. Electron Phys.* **35**, 87 (1974).
- ¹⁴L. M. Lidsky, S. D. Rothleder, D. J. Rose, S. Yoshikawa, C. Kichelson, and R. J. Mackin, *J. Appl. Phys.* **33**, 2490 (1962).
- ¹⁵For more information about the ANSYS code, contact ANSYS, Inc., Southpointe, 275 Technology Drive, Canonsburg, PA, 15317.
- ¹⁶S. M. Rossnagel, *J. Vac. Sci. Technol. A* **6**, 19 (1988).
- ¹⁷See Ref. 11, pp. 77–90.
- ¹⁸M. A. Lieberman and A. J. Lichtenberg, *Principles of Plasma Discharge and Material Processing* (Wiley and Sons, New York 1994).
- ¹⁹R. J. Goldston and P. H. Rutherford, *Introduction to Plasma Physics* (IOP, Bristol, UK, 1995).
- ²⁰S. Chandrasekhar, *Rev. Mod. Phys.* **15**, 1 (1943).
- ²¹A. E. Wendt and M. A. Lieberman, *J. Vac. Sci. Technol. A* **8**, 902 (1990).
- ²²E. W. McDaniel, *Collision Phenomena in Ionized Gases* (Wiley, New York, 1964).
- ²³S. Brown, *Basic Data of Plasma Physics* (MIT Press, Cambridge, MA, 1966).
- ²⁴J. A. Samson, *Vacuum Ultraviolet Spectroscopy* (Wiley, New York, 1965).